





Direct microstability optimization of stellarator devicesR. Jorge ^{1,2,*} W. Dorland ^{3,4,5} P. Kim ³ M. Landreman,⁴ N. R. Mandell ⁵ G. Merlo,⁶ and T. Qian⁵¹*Instituto de Plasmas e Fusão Nuclear, Instituto Superior Técnico, Universidade de Lisboa, 1049-001 Lisboa, Portugal*²*Department of Physics, University of Wisconsin-Madison, Madison, Wisconsin 53706, USA*³*Department of Physics, University of Maryland, College Park, Maryland 20742, USA*⁴*Institute for Research in Electronics and Applied Physics, University of Maryland, College Park, Maryland 20742, USA*⁵*Princeton Plasma Physics Laboratory, Princeton, New Jersey 08543, USA*⁶*Oden Institute for Computational Engineering and Sciences, The University of Texas at Austin, Austin, Texas 78712, USA*

(Received 16 May 2024; accepted 7 August 2024; published 3 September 2024)

Turbulent transport is regarded as one of the key issues in magnetic confinement nuclear fusion, both for tokamaks and stellarators. In this work, we show that a significant decrease in a microstability-based proxy, as opposed to a geometric one, for the turbulent heat flux, namely the quasilinear heat flux, can be obtained in an efficient manner by coupling stellarator optimization with linear gyrokinetic simulations. This is accomplished by computing the quasilinear heat flux at each step of the optimization process, as well as the deviation from quasisymmetry, and minimizing their sum, leading to a balance between neoclassical and the turbulent transport proxy.

DOI: [10.1103/PhysRevE.110.035201](https://doi.org/10.1103/PhysRevE.110.035201)**I. INTRODUCTION**

The stellarator is a class of fusion devices that can run in a steady state due to the flexible shaping of the confining magnetic field and the absence of current-driven instabilities [1]. This inherent flexibility allows stellarators to be optimized for a wide range of parameters, with W7-X [2] and HSX [3] examples of the experimental realizations of such optimization studies. One of the main difficulties in stellarator optimization is the balance between neoclassical transport, driven by trapped particles in a low collisionality regime, and turbulent transport in the core, the latter being driven largely by microinstabilities [4]. As an example, while W7-X has successfully shown decreased neoclassical transport, as in the tokamak case, turbulent transport is still limiting its energy confinement time [5]. Indeed, turbulent transport is currently one of the main limiting factors in the performance of magnetic confinement fusion devices. Although we are currently able to predict turbulent transport in the core with moderate accuracy, we still need an effective way to design machines with low turbulent transport, specifically, microinstability-driven turbulent transport [4,6].

In this work, we directly target both (1) the reduction of the microinstability drive of turbulent transport, and (2) the trapped particle losses driving neoclassical transport. As we show here, depending on the weights used in the optimization, a balance between the two types of transport is possible, and magnetic field equilibria with reduced quasilinear heat flux can be achieved. While previous optimization methods targeted cost functions based on proxy functions relying solely on the properties of the magnetic field equilibrium [7–9],

here, we do not rely on geometry-based proxy functions to evaluate microstability and directly solve the gyrokinetic equation at each iteration. This study shows gyrokinetic calculations performed within the optimization at every iteration. We note that, while in this study a particular numerical tool is used to solve the gyrokinetic equation and extract its linear growth rates and eigenfunctions, the direct optimization method employed here can be applied to other equilibrium and gyrokinetic codes which model different instability types and can easily be generalized to directly optimize turbulent heat and particle fluxes.

The framework used in this work to assess microstability is gyrokinetics. This is considered to be one of the main tools to assess the stability of fusion devices at spatial scales on the order of, or smaller than, the ion gyroradius ρ_i and at frequencies lower than the ion gyrofrequency Ω_i [10–12] and is usually regarded as the most complete, yet numerically efficient, framework to treat strongly magnetized plasmas [13]. For this reason, we quantify instabilities in this work by solving the linearized gyrokinetic equation to obtain the growth rates and corresponding eigenfunctions associated with the underlying instabilities. The instability studied here is the ion-temperature-gradient (ITG) mode, which is commonly regarded as one of the most transport-relevant electrostatic instabilities in tokamaks and stellarators [14,15].

The ITG mode develops on the ion gyroscale and is widely recognized as one of the main candidates to explain the experimental observations of anomalous ion heat turbulent transport in the core of fusion devices [16] as corroborated by numerical simulations [17–19]. The study of solely ion-driven instabilities such as the ITG mode is performed by removing the fast electron dynamics induced by electron inertia, meaning that the electron density in our model follows the perturbed electrostatic potential ϕ via the Boltzmann response. The

*Contact author: rogerio.jorge@wisc.edu

ITG mode can also deteriorate plasma confinement in electron heating scenarios by creating ion temperature clamping in low-power W7-X ECRH-only discharges without the use of the pellet injection or the boron dropper, preventing the heating of ions in the plasma core above 2 keV [20]. While ITG can drive a certain amount of electron heat flux (usually proportional to the driven ion heat flux), contributions to the electron heat flux from trapped electron modes are expected if the ITG is not sufficient to drive the electron heat flux imposed by the applied heating power [21].

As an optimization criterion to stabilize the underlying unstable modes, we choose our objective function J to be a quasilinear estimate [4,22] for the heat flux f_Q with the growth rates γ and associated eigenfunctions calculated using linear gyrokinetic simulations. The method employed here can also be used with nonlinear gyrokinetic or fluid codes by replacing the quasilinear estimate f_Q with the nonlinear heat flux Q computed by the respective code. This differs from previous objective functions that also targeted the reduction of turbulent transport such as Refs. [7,9,23] as these are solely based on properties of the equilibrium magnetic field and not on direct evaluations of gyrokinetic simulations, therefore requiring more assumptions about the geometry and the underlying modes. We note that, while the peak growth rate γ could be chosen as the objective function, we found it not to be a reliable indicator of the nonlinear heat flux due to the importance of smaller wave numbers [24]. The reduction of neoclassical transport is performed by targeting quasisymmetry, an invariance of the magnetic field strength B that guarantees confinement of the collisionless trajectories up to a threshold energy [25]. As shown in Ref. [26], it is indeed possible to design stellarators with precise quasisymmetry and achieve unprecedented levels of collisionless particle confinement and collisional transport for a thermal plasma. We leverage such findings by adding to the objective function J the term f_{QS} defined in Eq. (1) of Ref. [26] as it is already in a form ready to be used in a least-squares optimization method and, unlike previous optimization metrics, it does not require the calculation of Boozer coordinates [27] at each optimization step. We note that the quasisymmetry metric f_{QS} is, in fact, a measure of the deviation of quasisymmetry. Therefore, during optimization, we seek to minimize f_{QS} .

II. METHOD

The growth rates γ are calculated using the GS2 code [28–30] that solves the gyrokinetic equation

$$\frac{dh}{dt} + v_{\parallel} \mathbf{b} \cdot \nabla h + \mathbf{v}_d \cdot \nabla h = C + \frac{qF_0}{T_0} \frac{\partial \chi}{\partial t}, \quad (1)$$

coupled with the quasineutrality condition and Ampère's law. In Eq. (1), F_0 is the equilibrium distribution function, $h = f - F_0(1 - q\phi/T_0)$ is the nonadiabatic part of the distribution function f , $\chi = \langle \phi - \mathbf{v} \cdot \mathbf{A}/c \rangle$ is the gyroaveraged gyrokinetic potential with ϕ the electrostatic potential, and \mathbf{A} is the magnetic vector potential. $d_t = \partial_t + (c/B)[\chi, \cdot]$ is the total time derivative with $[\chi, h] = \partial \chi / \partial \mathbf{R} \times \partial h / \partial \mathbf{R} \cdot \mathbf{b}$ being the Poisson bracket, $\mathbf{v}_d = (\mathbf{b}/2\Omega_0) \times (2v_{\parallel}^2 \mathbf{b} \cdot \nabla \mathbf{b} + v_{\perp}^2 \nabla B_0/B_0)$ is the drift velocity with B_0 being the equilibrium magnetic field, $\Omega_0 = qB_0/m$ is the gyrofrequency with q the particle's charge and m its mass, and C is the gyroaveraged collision

operator. To focus on ITG modes, we reduce the gyrokinetic equation to its linear electrostatic flux-tube limit employing the adiabatic electron approximation, solve it as an initial value problem, and fit the temporal evolution of the absolute value of the electrostatic potential to an exponential of the form $\exp(\gamma t)$ with γ the growth rate.

The GS2 code employs a Fourier decomposition of the physical quantities in the x (normal) and y (binormal) directions with $\mathbf{k}_{\perp} = k_x \nabla x + k_y \nabla y$ the perpendicular wave vector and $\mathbf{r} = (x, y, z)$ the spatial coordinates. Such coordinates are based on the Clebsch representation for the equilibrium magnetic field $\mathbf{B} = \nabla \psi \times \nabla \alpha$ with ψ the toroidal magnetic flux and α a field line label on the flux surface defined in Boozer coordinates (ψ, θ, φ) as $\alpha = \theta - \iota \varphi$ with $\iota = d\theta/d\varphi$ [1]. The coordinates are then defined as $x = a\sqrt{s}$ with a a reference length taken here as the effective minor radius of the stellarator (see definition in page 12 of Ref. [31]) and $s = \psi/\psi_b$ where ψ_b is the value of ψ at the outermost flux surface (otherwise known as plasma boundary), $y = x\alpha$ and z a dimensionless coordinate along the field line.

The density and temperature profiles are assumed to decay exponentially in x with a constant scale length $L_n/a = -d \ln n/dx$ and $L_T/a = -d \ln T/dx$, respectively. For this work, we simulate flux tubes with $s = 0.25$ and linearly evolve modes with $k_x = \alpha = 0$ with a grid of ten values of $0.3 \leq k_y \leq 3.0$. However, we note that while the choice $\alpha = 0$ is expected to lead to a peak of the modes mainly on the outboard side [19] where the choice $k_x = 0$ is likely to yield growth rates at or close to the maximum one, this hypothesis, when applied to the design of new devices, should be corroborated *a posteriori* via nonlinear simulations at finite k_y and k_x . The density and temperature profiles used are $a/L_n = 1$ and $a/L_T = 3$, respectively, with a the minor radius, leading to $\eta = L_T/L_n = 3$, a typically used value in cyclone base case scenarios [32]. The remaining input parameters for GS2 were obtained by performing convergence tests for the initial and final equilibria of each optimization in a similar fashion to Ref. [33]. In particular, we use a total of five poloidal turns, 151 points along the field line and 35 points along the velocity pitch angle variable λ .

We then write the quasi-linear estimate f_Q for the heat flux using a mixing length saturation rule [34]

$$f_Q = \sum_{k_y} \frac{\gamma(k_y)}{\langle k_{\perp}^2(k_y) \rangle}, \quad (2)$$

where the sum is taken over all values of k_y used in the simulation, and $\langle k_{\perp}^2 \rangle = \int g^{yy} k_y^2 |\hat{\phi}|^2 \sqrt{g} dz / \int |\hat{\phi}|^2 \sqrt{g} dz$ is the flux-surface average of the squared perpendicular wave number with $|\hat{\phi}|$ the amplitude of the mode and \sqrt{g} the Jacobian. As shown in Ref. [4], such a quasilinear transport model overcomes some of the limitations of the heuristic mixing length estimate γ/k_y^2 by taking into account the extension of the toroidal modes along z .

The components of the magnetic field equilibrium relevant to compute both the geometric coefficients entering Eq. (1) and the quasisymmetry objective function f_{QS} are calculated using the variational moments equilibrium code (VMEC) [35]. VMEC finds a solution of ideal magnetohydrodynamics (MHD) equation $\mathbf{J} \times \mathbf{B} = \nabla P$,

with $\mathbf{J} = \nabla \times \mathbf{B}/\mu_0$ the plasma current and P the plasma pressure, by applying a variational method to the integral form of the MHD equations. We run VMEC in fixed-boundary mode where an MHD equilibrium is obtained by specifying the last closed flux surface S as boundary condition parametrized by two variables (θ, ϕ) , namely an anglelike variable termed the poloidal angle θ and the standard cylindrical toroidal angle ϕ , respectively, allowing us to define $S = [R(\theta, \phi) \cos(\phi), R(\theta, \phi) \sin(\phi), Z(\theta, \phi)]$ where $R = \sum_{m=0}^{M_{\text{pol}}} \sum_{n=-N_{\text{tor}}}^{N_{\text{tor}}} \text{RBC}_{m,n} \cos(m\theta - n_{\text{tp}}n\phi)$ and $Z = \sum_{m=0}^{M_{\text{pol}}} \sum_{n=-N_{\text{tor}}}^{N_{\text{tor}}} \text{ZBS}_{m,n} \sin(m\theta - n_{\text{tp}}n\phi)$. In the Fourier decompositions of R and Z , the sin and cos terms are set to zero, respectively, to ensure stellarator-symmetry [36] and n_{tp} is the toroidal periodicity of the equilibrium. While stellarator symmetry is, in principle, not necessary, it allows us to restrict the total number of degrees of freedom while still providing adequate optimized solutions. Given a plasma boundary S , a plasma pressure profile $P(\psi)$, and a net toroidal current I , VMEC seeks a solution of the ideal MHD system of equations with nested closed flux surfaces.

The optimization algorithm, the calculation of the quasisymmetry objective function, and the calculation of the geometric coefficients that enter the gyrokinetic equation are performed using the SIMSOPT code [37]. The independent variables for optimization are the boundary Fourier coefficients $\{\text{RBC}_{m,n}, \text{ZBS}_{m,n}\}$ excluding $\text{RBC}_{0,0}$ which is set to one to fix the spatial scale. We use as initial condition the precise quasihelically (QH) symmetric configuration of Ref. [26] with $n_{\text{fp}} = 4$ and set to zero all surface modes with $m \geq 1$ and $|n| \geq 1$. Finally, in order to keep the same aspect ratio as the provided initial condition to the optimization, we add to the objective function J the term $f_A = (A - A^*)^2$ where A is the aspect ratio of the configuration computed at each iteration and $A^* = 8$ the target (initial) aspect ratio. The final objective function is then given by

$$J = \omega_{f_Q} f_Q + f_{\text{QS}} + f_A, \quad (3)$$

where ω_{f_Q} is the weight given to the minimization of f_Q .

III. RESULTS

We first perform a parameter space scan to guide the choice of our optimization algorithm. Namely, we assess the dependence of the quasisymmetry cost function f_{QS} and the quasilinear estimate f_Q on the geometry of the magnetic field by performing a scan on the $\text{RBC}_{0,1}$ boundary mode in the range $(-0.2, 0.2)$, a range of values where VMEC is able to yield converged with a tolerance of $\text{FTOL} = 10^{-14}$ with 131 radial points within 7000 iterations on the initial QH configuration where $\text{RBC}_{0,1} = 0.180$. This is shown in Fig. 1 with the value of f_Q illustrating microstability in blue and the value of f_{QS} illustrating quasisymmetry in orange. We find that while there are only two local minima of f_{QS} , the cost function f_Q contains many local minima with its global minimum at a different location than the global minimum of f_{QS} . Therefore, when performing optimization studies on both quasisymmetry and microstability, a compromise on the level of quasisymmetry is expected. Given the fact that the local minima of f_Q and f_{QS} appear to be well separated, and that the roughness of the cost function f_Q does not lead

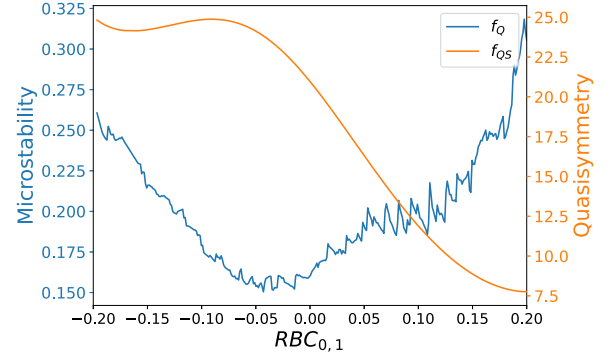


FIG. 1. Quasilinear estimate f_Q (noisy, lower line) and quasisymmetry cost function f_{QS} (smooth, upper line) as a function of the surface shape parameter $\text{RBC}_{0,1}$ for the quasihelically symmetric configuration used as initial conditions for the optimization.

to large jumps in f_Q for small changes of $\text{RBC}_{0,1}$, we use a local optimization algorithm instead of a global optimization algorithm. This leads to a more efficient optimization method but it may not result in the global minimum of the objective function found. However, as it is shown below, the solution found is able to fulfill our desired criteria. The optimization is carried out using the Python library Scipy [38] for nonlinear least-squares minimization by employing the Levenberg-Marquardt method. Gradients are computed using finite differences, with Message Passing Interface (MPI) for concurrent function evaluations where, at each iteration, both the magnetic field inside the boundary (using VMEC) and the gyrokinetic simulations (using GS2) are computed within the SIMSOPT framework. In order to steer the optimizer away from the many local minima present in f_Q and still be able to use finite differences, we use a large value for the relative Δ_r and absolute Δ_a step sizes and perform two extra optimization to refine the minimum found. Due to the smallness of the degrees of freedom with increasing Fourier modes, for a given maximum mode M_{pol} , we use $\Delta_r = 0.015/M_{\text{pol}}$ and $\Delta_a = \min[0.003, (M_{\text{pol}}/5) \times 10^{-M_{\text{pol}}}]$ in the first optimization, then decreasing Δ_r and Δ_a by a factor of 10 and 300 for the two ensuing optimizations, respectively. We note that the study in Fig. 1 is performed by varying a single parameter and the extrapolation of such findings to other optimization parameters would need a multi-dimensional survey. Therefore, an *a posteriori* examination of the growth rates and is performed to assess the effectiveness of this optimization procedure.

We perform five optimization studies. The first targets only quasisymmetry by setting $\omega_{f_Q} = 0$ and will be used as a benchmark case. The resulting optimization is shown in Fig. 2 (left). The remaining studies target both microstability and quasisymmetry simultaneously and set $\omega_{f_Q} = 0.1, 1, 10,$ and 100 . The resulting optimization for the value of $\omega_{f_Q} = 10$ is shown in Fig. 2 (right). The overall optimization was done in an iterative fashion, namely, an optimization with large and smaller step sizes was performed at each of maximum surface Fourier modes $M_{\text{pol}} = N_{\text{tor}} = 1, 2, 3, 4$. A further increase of M_{pol} and N_{tor} resulted in negligible improvements in the objective function in the $\omega_{f_Q} = 10$ case. Therefore, the resulting configurations have only surface Fourier modes up to $m \leq 4$ and $|n| \leq 4$.

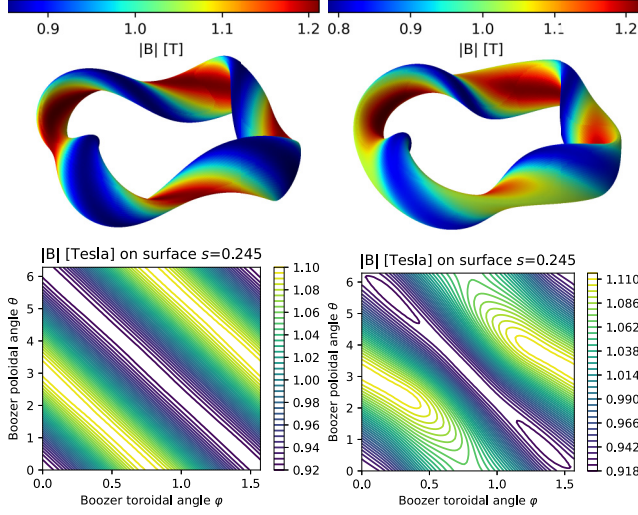


FIG. 2. Top: Magnetic field configuration optimized for quasisymmetry with $\omega_{f_Q} = 0$ (left) and the configuration optimized for quasisymmetry and microstability with $\omega_{f_Q} = 10$ (right) where the color shows the magnetic field strength on that surface. Bottom: Field strength on an $s = 0.245$ flux surface in Boozer coordinates for $\omega_{f_Q} = 0$ (left) and $\omega_{f_Q} = 10$ (right).

The initial values of f_{QS} and f_Q are 1.412×10^{-1} and 1.346×10^{-1} , respectively. We find that, for the cases of $\omega_{f_Q} = 0, 0.1, 1, 10$, and 100 , the quasisymmetry objective function increases from $f_{QS} = 2 \times 10^{-4}$ to 4×10^{-4} ,

1.11×10^{-2} , 1.171×10^{-1} , and 2.966×10^{-1} , respectively, while the microstability objective function decreases from $f_Q = 1.92 \times 10^{-1}$ to 1.91×10^{-1} , 1.63×10^{-1} , 1.12×10^{-1} and 1.01×10^{-1} , respectively. In order to assess the deterioration in quasisymmetry, we show in Fig. 2 (bottom) the contours of the magnetic field strength at $s = 0.245$ with the deviation from straight lines appearing in the second case (optimization for microstability). On the other hand, the enhanced microstability properties of the resulting configuration are evident even at values of L_n and L_T outside the ones used for the optimization, and for several flux tubes and radii, see Fig. 3.

The properties of the five different configurations obtained from the optimizations at $\omega_{f_Q} = 0, 0.1, 1, 10$, and 100 are now assessed. We compare in Fig. 4 the rotational transform ι (top left), cross sections at a cylindrical angle $\phi = 0$ (top right), and geometry coefficient $|\nabla\psi|^2$ (bottom) between the different configurations. We find that, as microstability is favored with increasing ω_{f_Q} , the rotational transform decreases and, comparing with $\omega_{f_Q} = 0$ and 0.1 , there is a finite magnetic shear. We note that magnetic shear has been associated with turbulence reduction, see Refs. [39–41]. Furthermore, it is found that the cross sections become more circular and, therefore, have less surface compression, as ω_{f_Q} is increased. Finally, as shown in Fig. 4 (bottom), the maxima of the metric tensor coefficient $|\nabla\psi|^2$ are seen to decrease as the value of ω_{f_Q} increases. This parameter represents flux surface compression and plays a role in ITG turbulence as it is the

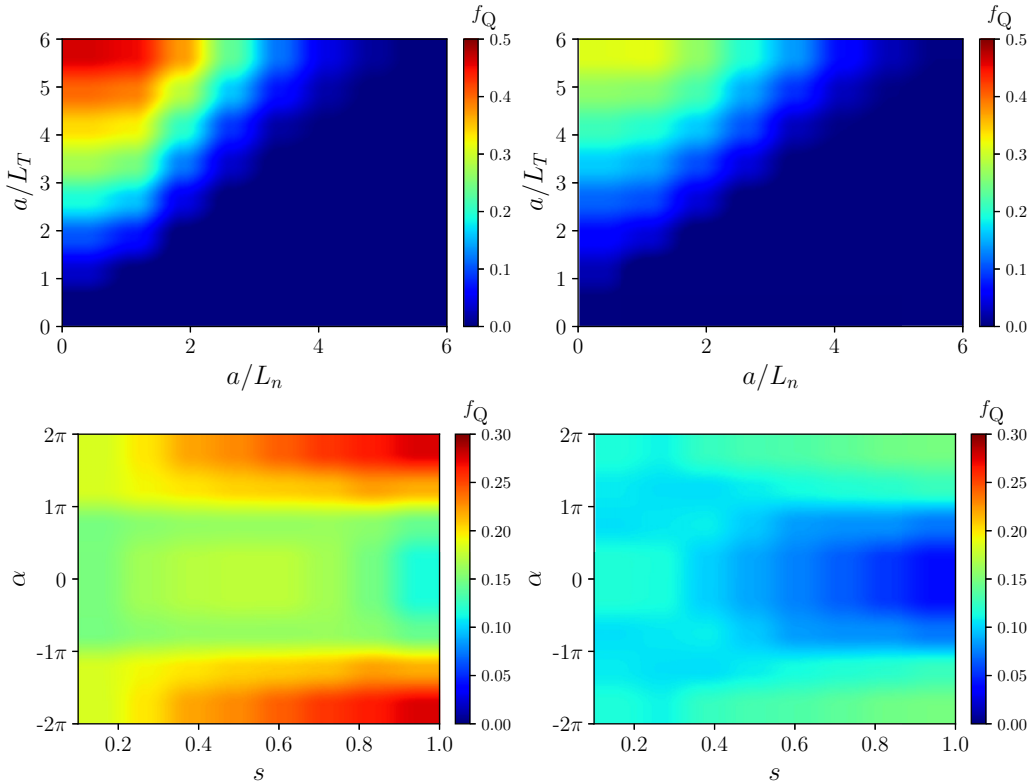


FIG. 3. Top: Comparison of the quasilinear estimate for the heat flux between the configuration optimized for $\omega_{f_Q} = 0$ (left) and $\omega_{f_Q} = 10$ (right) for several profile scale lengths L_n and L_T . We note that the stability (dark blue color) observed in the lower right corners is a characteristic of the adiabatic electron assumption employed here. Bottom: Similar comparison at fixed $a/L_n = 1$ and $a/L_T = 3$ for different field line labels α and surfaces s corresponding to different fluxtubes.

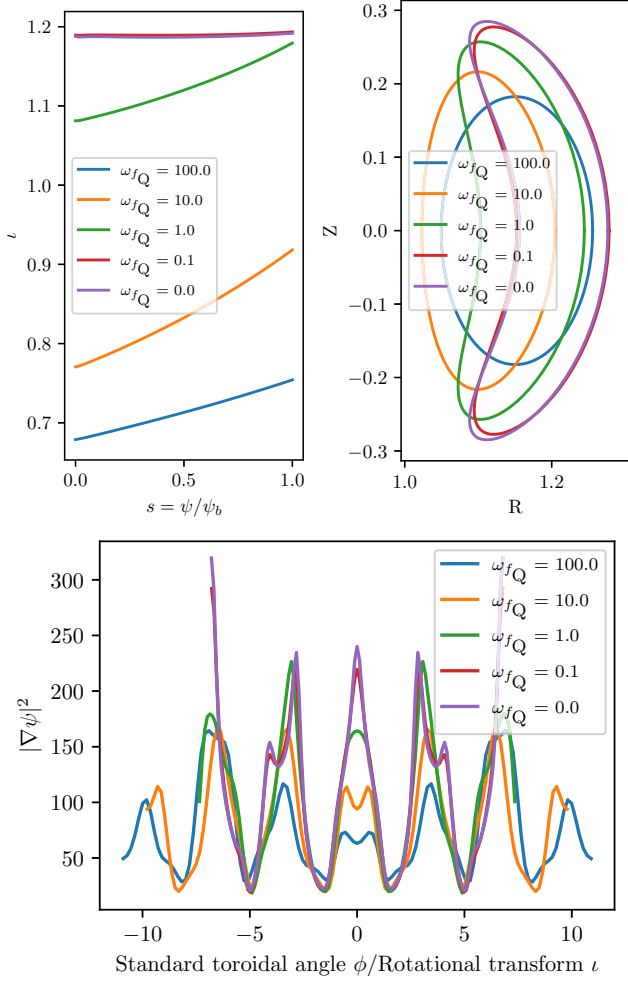


FIG. 4. Radial profiles of rotational transform ι (top left), cross-sectional cuts of the plasma boundary at cylindrical angle $\phi = 0$ and metric tensor coefficient $g^{\psi\psi} = |\nabla\psi|^2$ along a field line (bottom) for the five optimization cases considered here at $\omega_{fQ} = 0, 0.1, 1, 10$ and 100 . R and Z are shown in units of the major radius R_0 , here taken as $R_0 = 1\text{m}$.

coefficient of the ion radial heat flux $Q_i \propto -|\nabla\psi|^2 dT_i/dx$ [7].

We now perform an *a posteriori* assessment of the neoclassical and quasilinear transport of the optimized configurations, free-boundary standard configuration of the W7-X device [42] and the free-boundary configuration of the HSX device [3]. Both the W7-X and HSX files consist of the vacuum configurations taken from the public repository in Ref. [43]. We start with a comparison of the quasilinear proxy f_Q between the five different optimizations and the W7-X device. This is shown in Fig. 5. Here we find that a precise QH configuration with four field periods has a larger quasilinear flux than W7-X. A similar conclusion holds for the maximum growth rates and for different flux tubes. However, the f_Q decreases to levels similar to W7-X for $\omega_{fQ} = 10$, and reaches even lower values for $\omega_{fQ} = 100$. Additionally, we note that the optimization performed here also led to similar, or possibly higher, f_Q critical gradient values of a/L_T for the case of $\omega_{fQ} = 10$ when compared with other values of ω_{fQ} .

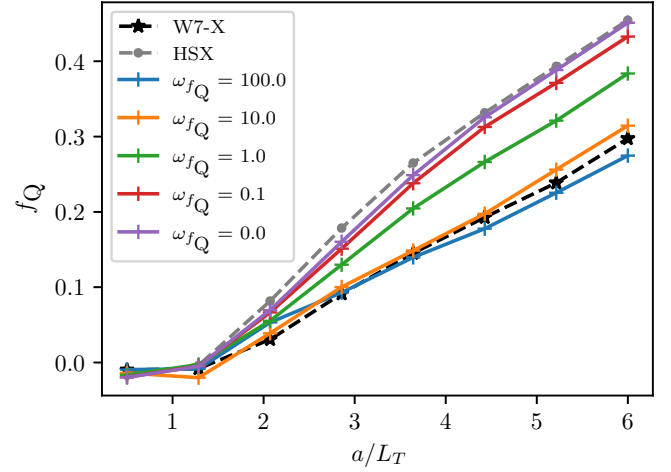


FIG. 5. Comparison of the quasilinear estimate f_Q from Eq. (2) between the standard configuration of W7-X, HSX, and the five optimizations carried out here at $\omega_{fQ} = 0, 0.1, 1, 10$ and 100 as a function of the minor radius a divided by the gradient scale length of the ion temperature a/L_T .

As a metric for neoclassical transport, we use the parameter ϵ_{eff} , as $\epsilon_{\text{eff}}^{3/2}$ scales with the diffusive transport of trapped particles in the long-mean-free-path collisionality regime. This quantity is computed using the NEO code [44]. In Fig. 6 (bottom) we show the value of ϵ_{eff} for the standard configuration of W7-X, HSX and the optimizations performed in this work. We see that the values of ϵ_{eff} for the $\omega_{fQ} = 10$ microstability optimized case is within the range of current optimized experiments such as the HSX [3] and W7-X [42] devices, with smaller (larger) ϵ_{eff} values for smaller (larger) ω_{fQ} , as expected. Regarding fast particle confinement, we assess in Fig. 6 (top) the fraction of lost particles to the surface by tracing the guiding center motion of 3500 test particles initialized isotropically on the $s = 0.25$ surface followed using the SIMPLE code [45] for 0.01s. For this case, the configurations are scaled to the same minor radius 1.7m and field strength on-axis of $B_0 = 5.7\text{T}$ of the ARIES-CS fusion reactor study, in a similar fashion as in Refs. [26,46]. We find that the optimization cases with ω_{fQ} up to $\omega_{fQ} = 1$ lead to no loss of particles, while optimizations with $\omega_{fQ} > 1$ have finite loss fractions, with a maximum of 4.5% at $\omega_{fQ} = 100$, showing that reducing ITG growth rates in QH stellarators comes at the expense of poor particle confinement due to the degradation of quasisymmetry.

IV. CONCLUSIONS

In this work, for the first time, microstability is taken into account in the optimization of quasisymmetric magnetic field configurations using first-principles gyrokinetic simulations. We were able to significantly reduce the quasilinear estimate for the heat flux, although at the cost of larger neoclassical transport. Notwithstanding, the resulting fast particle loss is still smaller than most stellarator designs to date and with similar levels of neoclassical transport. An extension of the framework introduced here to directly optimize for turbulent transport by replacing a quasilinear estimate for the heat flux

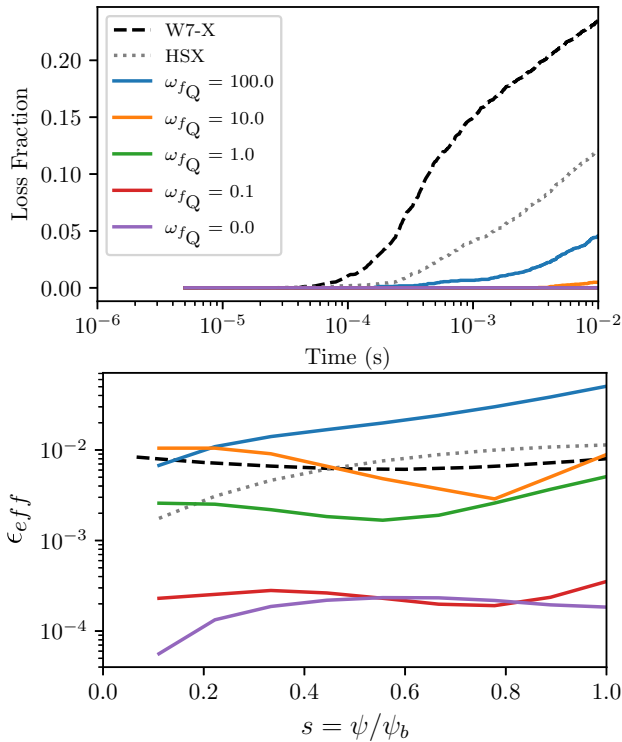


FIG. 6. Top: Fraction of 3.5 MeV alpha particles from a total of 3500 that are lost at 0.01s the plasma boundary $s = 1$ when started isotropically at $s = 0.25$. Bottom: Relative levels of neoclassical transport for a thermal plasma in the $1/\nu$ regime, measured using the effective helical ripple quantity ϵ_{eff} , between the configurations found in this work and two of the most recently built stellarators, the quasihelical symmetric HSX machine and the quasi-isodynamic W7-X machine.

with its nonlinear counterpart will be the subject of future work. Furthermore, additional optimization targets, such as MHD stability, can be added to the objective function used, which might impose additional constraints on the magnetic field geometry.

The data supporting this study's findings are available in Zenodo [47].

ACKNOWLEDGMENTS

We thank A. Goodman for fruitful discussions as well as the GS2 and SIMSOPT teams for their invaluable contributions. This work has been carried out within the framework of the EUROfusion Consortium, funded by the European Union via the Euratom Research and Training Programme (Grant Agreement No 101052200–EUROfusion). IST activities also received financial support from FCT - Fundação para a Ciência e Tecnologia through Projects No. UIDB/50010/2020 and No. UIDP/50010/2020. R.J. is supported by the Portuguese FCT-Fundação para a Ciência e Tecnologia, under Grant No. 2021.02213. CEECIND and [48] and by the EUROfusion Enabling Research project (ENR-MOD.01.IST). N.R.M. was supported by the US DOE Fusion Energy Sciences Postdoctoral Research Program administered by the Oak Ridge Institute for Science and Education (ORISE) for the DOE via Oak Ridge Associated Universities (ORAU) under DOE Contract No. DE-SC0014664. T.Q. is supported by the NSF Graduate Research Fellowship Program Grant No. DGE-2039656.

The optimization studies were carried out using the EUROfusion Marconi supercomputer facility. Views and opinions expressed here are those of the author(s) only and do not necessarily reflect those of the European Union, the European Commission, DOE, NSF, ORAU, or ORISE. None of these parties can be held responsible for them.

- [1] P. Helander, Theory of plasma confinement in non-axisymmetric magnetic fields, *Rep. Prog. Phys.* **77**, 087001 (2014).
- [2] J. Geiger, C. D. Beidler, Y. Feng, H. Maassberg, N. B. Marushchenko, and Y. Turkin, Physics in the magnetic configuration space of W7-X, *Plasma Phys. Control. Fusion* **57**, 014004 (2015).
- [3] F. S. B. Anderson, A. F. Almagri, D. T. Anderson, P. G. Matthews, J. N. Talmadge *et al.*, The helically symmetric experiment, (HSX) goals, design and status, *Fusion Technol.* **27**, 273 (1995).
- [4] F. Jenko, T. Dannert, and C. Angioni, Heat and particle transport in a tokamak: Advances in nonlinear gyrokinetics, *Plasma Phys. Control. Fusion* **47**, B195 (2005).
- [5] C. D. Beidler, H. M. Smith, A. Alonso, T. Andreeva, J. Baldzuhn *et al.*, Demonstration of reduced neoclassical energy transport in Wendelstein 7-X, *Nature (London)* **596**, 221 (2021).
- [6] C. Holland, L. Schmitz, T. L. Rhodes, W. A. Peebles, J. C. Hillesheim *et al.*, Advances in validating gyrokinetic turbulence models against L- and H-mode plasmas a, *Phys. Plasmas* **18**, 056113 (2011).
- [7] H. E. Mynick, N. Pomphrey, and P. Xanthopoulos, Optimizing stellarators for turbulent transport, *Phys. Rev. Lett.* **105**, 095004 (2010).
- [8] P. Xanthopoulos, H. E. Mynick, P. Helander, Y. Turkin, G. G. Plunk *et al.*, Controlling turbulence in present and future stellarators, *Phys. Rev. Lett.* **113**, 155001 (2014).
- [9] G. T. Roberg-Clark, P. Xanthopoulos, and G. G. Plunk, Reduction of electrostatic turbulence in a quasi-helically symmetric stellarator via critical gradient optimization, *J. Plasma Phys.* **90**, 175900301 (2024).
- [10] P. J. Catto, Linearized gyro-kinetics, *Plasma Phys.* **20**, 719 (1978).
- [11] T. M. Antonsen, Jr. and B. Lane, Kinetic equations for low frequency instabilities in inhomogeneous plasmas, *Phys. Fluids* **23**, 1205 (1980).
- [12] E. A. Frieman, G. Rewoldt, W. M. Tang, and A. H. Glasser, General theory of kinetic ballooning modes, *Phys. Fluids* **23**, 1750 (1980).
- [13] P. Helander and G. G. Plunk, Upper bounds on gyrokinetic instabilities in magnetized plasmas, *Phys. Rev. Lett.* **127**, 155001 (2021).

- [14] W. Horton, Drift waves and transport, *Rev. Mod. Phys.* **71**, 735 (1999).
- [15] P. Helander, J. H. E. Proll, and G. G. Plunk, Collisionless microinstabilities in stellarators. I. Analytical theory of trapped-particle modes, *Phys. Plasmas* **20**, 122505 (2013).
- [16] X. Garbet, P. Mantica, C. Angioni, E. Asp, Y. Baranov *et al.*, Physics of transport in tokamaks, *Plasma Phys. Control. Fusion* **46**, B557 (2004).
- [17] T. S. Hahm and W. M. Tang, Properties of ion temperature gradient drift instabilities in H-mode plasmas, *Phys. Fluids B* **1**, 1185 (1989).
- [18] F. Romanelli, Ion temperature-gradient-driven modes and anomalous ion transport in tokamaks, *Phys. Fluids B* **1**, 1018 (1989).
- [19] G. G. Plunk, P. Helander, P. Xanthopoulos, and J. W. Connor, Collisionless microinstabilities in stellarators. III. The ion-temperature-gradient mode, *Phys. Plasmas* **21**, 032112 (2014).
- [20] M. N. A. Beurskens, S. A. Bozhnikov, O. Ford, P. Xanthopoulos, A. Zocco *et al.*, Ion temperature clamping in Wendelstein 7-X electron cyclotron heated plasmas, *Nucl. Fusion* **61**, 116072 (2021).
- [21] F. Ryter, C. Angioni, M. Dunne, R. Fischer, B. Kurzan *et al.*, Heat transport driven by the ion temperature gradient and electron temperature gradient instabilities in ASDEX upgrade H-modes, *Nucl. Fusion* **59**, 096052 (2019).
- [22] E. Fable, C. Angioni, and O. Sauter, The role of ion and electron electrostatic turbulence in characterizing stationary particle transport in the core of tokamak plasmas, *Plasma Phys. Control. Fusion* **52**, 015007 (2009).
- [23] J. H. E. Proll, H. E. Mynick, P. Xanthopoulos, S. A. Lazerson, and B. J. Faber, TEM turbulence optimisation in stellarators, *Plasma Phys. Control. Fusion* **58**, 014006 (2015).
- [24] M. J. Pueschel, B. J. Faber, J. Citrin, C. C. Hegna, P. W. Terry, and D. R. Hatch, Stellarator turbulence: Subdominant eigenmodes and quasilinear modeling, *Phys. Rev. Lett.* **116**, 085001 (2016).
- [25] J. Nührenberg and R. Zille, Quasi-helically symmetric toroidal stellarators, *Phys. Lett. A* **129**, 113 (1988).
- [26] M. Landreman and E. Paul, Magnetic fields with precise quasisymmetry for plasma confinement, *Phys. Rev. Lett.* **128**, 035001 (2022).
- [27] A. H. Boozer, Plasma equilibrium with rational magnetic surfaces, *Phys. Fluids* **24**, 1999 (1981).
- [28] M. Kotschenreuther, G. Rewoldt, and W. M. Tang, Comparison of initial value and eigenvalue codes for kinetic toroidal plasma instabilities, *Comput. Phys. Commun.* **88**, 128 (1995).
- [29] W. Dorland, F. Jenko, M. Kotschenreuther, and B. N. Rogers, Electron temperature gradient turbulence, *Phys. Rev. Lett.* **85**, 5579 (2000).
- [30] J. A. Baumgaertel, E. A. Belli, W. Dorland, W. Guttenfelder, G. W. Hammett *et al.*, Simulating gyrokinetic microinstabilities in stellarator geometry with GS2, *Phys. Plasmas* **18**, 122301 (2011).
- [31] M. Landreman and W. Sengupta, Constructing stellarators with quasisymmetry to high order, *J. Plasma Phys.* **85**, 815850601 (2019).
- [32] A. M. Dimits, G. Bateman, M. A. Beer, B. I. Cohen, W. Dorland *et al.*, Comparisons and physics basis of tokamak transport models and turbulence simulations, *Phys. Plasmas* **7**, 969 (2000).
- [33] R. Jorge and M. Landreman, Ion-temperature-gradient stability near the magnetic axis of quasisymmetric stellarators, *Plasma Phys. Control. Fusion* **63**, 074002 (2021).
- [34] A. Mariani, S. Brunner, J. Dominski, A. Merle, G. Merlo *et al.*, Identifying microturbulence regimes in a TCV discharge making use of physical constraints on particle and heat fluxes, *Phys. Plasmas* **25**, 012313 (2018).
- [35] S. P. Hirshman and J. C. Whitson, Steepest-descent moment method for three-dimensional magnetohydrodynamic equilibria, *Phys. Fluids* **26**, 3553 (1983).
- [36] R. L. Dewar and S. R. Hudson, Stellarator symmetry, *Physica D* **112**, 275 (1998).
- [37] M. Landreman, B. Medasani, F. Wechsung, A. Giuliani, R. Jorge *et al.*, SIMSOPT: A flexible framework for stellarator optimization, *J. Open Source Software* **6**, 3525 (2021).
- [38] P. Virtanen, R. Gommers, T. E. Oliphant, M. Haberland, T. Reddy *et al.*, SciPy 1.0: fundamental algorithms for scientific computing in Python, *Nat. Methods* **17**, 261 (2020).
- [39] P. Xanthopoulos, G. G. Plunk, A. Zocco, and P. Helander, Intrinsic turbulence stabilization in a stellarator, *Phys. Rev. X* **6**, 021033 (2016).
- [40] G. G. Plunk, P. Xanthopoulos, and P. Helander, Distinct turbulence saturation regimes in stellarators, *Phys. Rev. Lett.* **118**, 105002 (2017).
- [41] B. J. Faber, M. J. Pueschel, P. W. Terry, C. C. Hegna, and J. E. Roman, Stellarator microinstabilities and turbulence at low magnetic shear, *J. Plasma Phys.* **84**, 905840503 (2018).
- [42] C. Beidler, G. Grieger, F. Herrnegger, E. Harmeyer, J. Kisslinger *et al.*, Physics and engineering design for Wendelstein VII-X, *Fusion Technology* **17**, 148 (1990).
- [43] M. Landreman, http://www.github.com/landreman/vmec_equilibria, GitHub, *vmec_equilibria* (2024).
- [44] V. V. Nemov, S. V. Kasilov, W. Kernbichler, and M. F. Heyn, Evaluation of $1/\nu$ neoclassical transport in stellarators, *Phys. Plasmas* **6**, 4622 (1999).
- [45] C. G. Albert, S. V. Kasilov, and W. Kernbichler, Accelerated methods for direct computation of fusion alpha particle losses within, stellarator optimization, *J. Plasma Phys.* **86**, 815860201 (2020).
- [46] A. Bader, M. Drevlak, D. T. Anderson, B. J. Faber, C. C. Hegna *et al.*, Stellarator equilibria with reactor relevant energetic particle losses, *J. Plasma Phys.* **85**, 905850508 (2019).
- [47] R. Jorge, Data for the paper “Direct Microstability Optimization of Stellarator Devices” [Data set], Zenodo (2020), <https://doi.org/10.5281/zenodo.7415457>.
- [48] <https://sciproj.ptcris.pt/7571EEC>